REGULARIZED COHERENCE ENHANCING FILTERING

Oľga Stašová — Zuzana Krivá

Slovak University of Technology, Bratislava, SLOVAKIA

ABSTRACT. The paper deals with the nonlinear tensor diffusion which yields a coherence improvement. It is very appropriate for images with flow-like structures. Two convolutions are used in the construction of diffusion tensor for such a model, see [Drblíková, O.—Mikula, K.: *Convergence analysis of finite volume scheme for nonlinear tensor anisotropic diffusion in image processing,* SIAM J. Numer. Anal. **46** (2007), 37–60], [Weickert, J.: *Coherence-enhancing diffusion filtering,* Int. J. Comput. Vis. **31** (1999), 111–127]. In this paper we introduce the third supplemental convolution in order to enhance the diffusion strategy.

First, we briefly present the classical coherence enhancing model and explain our modification. Then the discrete scheme is provided. The core of the paper consists in numerical experiments. Benefits of the additional convolution are discussed and illustrated in the figures.

1. Introduction

Coherence enhancing diffusion (CED), see [10], is a recovery technique which improves a connectivity of image structures. It possesses the capability to close gaps in the structures since the diffusion tensor supports the diffusion in the direction of edges, see Fig. 1. On the other hand, the filtering is kept low in the perpendicular direction to avoid blurring edges. The CED is often used as a pre-processing algorithm for methods such as the edge detection and segmentation which produce significantly better results after the improvement of image structural connectivity. This approach can be also applied as a post-processing technique.

FIGURE 1. The image on the left has been processed by the coherence enhancing diffusion. The algorithm CED3 discussed in this paper has been used. The coherence of disrupted structures has been improved while small isolated spots have been removed.

2. Mathematical model

The coherence enhancing diffusion model has the following form, see [3, 10],

$$\frac{\partial u}{\partial t} - \nabla \cdot (D\nabla u) = 0 \qquad \text{in } Q_T \equiv \Omega \times I, \tag{1}$$

$$u(x, 0) = u_0(x) \qquad \text{in } \Omega, \tag{2}$$

$$D\nabla u \cdot \mathbf{n} = 0 \qquad \text{on } \partial\Omega \times I, \tag{3}$$

where $u(x, t)$ is an unknown function and denotes a grey level image intensity, $u_0 \in L^2(\Omega)$, $\mathbf{n}$ denotes the outer normal unit vector to the $\partial\Omega$ and the matrix $D = D(x, t)$ is the diffusion tensor, which leads the filtering. We consider this problem on the spatio-temporal domain Q_T, where Ω represents a rectangular image domain with boundary $\partial\Omega$ and $I = [0, T]$ is a time interval.

2.1. Diffusion tensor

The design of the diffusion tensor is based on the eigenvalues and eigenvectors of the so-called structure tensor

$$J_\rho(\nabla u_{\tilde{t}}) = G_\rho * (\nabla u_{\tilde{t}} \nabla u_{\tilde{t}}^T) = \begin{pmatrix} a & b \\ b & c \end{pmatrix},$$

where

$$u_{\tilde{t}}(x, t) = \big(G_{\tilde{t}} * u(\cdot, t)\big)(x) \tag{4}$$

and $G_{\tilde{t}}$ and G_ρ are Gaussian kernels. Parameters $\tilde{t}$ and ρ are positive.

The choice of $\tilde{t}$ and ρ depends on the image data. The noise scale $\tilde{t}$ ensures that the details smaller than $O(\tilde{t})$ are ignored by the edge detector. The integration scale ρ should be chosen following the characteristic texture size. Usually, it is large in comparison to the noise scale $\tilde{t}$, see [11]. The matrix J_ρ satisfies symmetry and positive semi-definiteness properties. Its eigenvectors are parallel and orthogonal to $\nabla u_{\tilde{t}}$. This matrix is also known as an interest operator or second moment matrix in computer vision, see [6]. Its eigenvalues are given as follows

$$\mu_{1,2} = \frac{1}{2}\left(a + c \pm \sqrt{(a-c)^2 + 4b^2}\right), \qquad \mu_1 \geq \mu_2. \tag{5}$$

The corresponding orthogonal set of eigenvectors (v, w) to eigenvalues (μ_1, μ_2) is given by

$$\begin{aligned}
\mathbf{v} &= (v_1, v_2), & \mathbf{w} &= (w_1, w_2), \\
v_1 &= 2b, & v_2 &= c - a + \sqrt{(a-c)^2 + 4b^2}, \\
\mathbf{w} &\perp \mathbf{v}, & w_1 &= -v_2, & w_2 &= v_1.
\end{aligned} \tag{6}$$

The orientation of the eigenvector $\mathbf{w}$, which corresponds to the smaller eigenvalue μ_2 is called the coherence orientation. The lowest image intensity fluctuations occur just in this orientation.

The diffusion tensor D is constructed to lead a diffusion such that the filtering is intense in the coherence direction $\mathbf{w}$ and increases with the coherence $(\mu_1 - \mu_2)^2$.

For this purpose, the eigenvectors of D are the same as the eigenvectors of the structure tensor $J_\rho(\nabla u_{\tilde{t}})$ labelled as $\mathbf{v}$ and $\mathbf{w}$ and the choice of diffusion tensor eigenvalues is the following

$$\kappa_1 = \alpha, \qquad \alpha \in (0,1), \qquad \alpha \ll 1, \tag{7}$$

$$\kappa_2 = \begin{cases} \alpha & \text{if } \mu_1 = \mu_2, \\ \alpha + (1-\alpha)\exp\left(\frac{-C}{(\mu_1 - \mu_2)^2}\right), \ C > 0 & \text{else.} \end{cases}$$

Then we acquire the diffusion tensor D in the following form

$$D = ABA^{-1} = \begin{pmatrix} D_{11} & D_{12} \\ D_{12} & D_{22} \end{pmatrix},$$

where

$$A = \begin{pmatrix} v_1 & -v_2 \\ v_2 & v_1 \end{pmatrix} \quad \text{and} \quad B = \begin{pmatrix} \kappa_1 & 0 \\ 0 & \kappa_2 \end{pmatrix} \tag{8}$$

which is non-linearly dependent on partial derivatives of solution u and fulfils smoothness, symmetry and uniform positive definiteness properties.

2.2. Regularized diffusion tensor

The construction of our diffusion tensor differs from the previous one only in the relation (8) which we replace by

$$D = G_\theta * (ABA^{-1}) = \begin{pmatrix} D_{11} & D_{12} \\ D_{12} & D_{22} \end{pmatrix},$$

where

$$A = \begin{pmatrix} v_1 & -v_2 \\ v_2 & v_1 \end{pmatrix} \quad \text{and} \quad B = \begin{pmatrix} \kappa_1 & 0 \\ 0 & \kappa_2 \end{pmatrix} \tag{9}$$

and G_θ is a Gaussian kernel. By our best knowledge, introduction of the third convolution is new in known literature.

In order to distinguish both coherence enhancing techniques below, we label the classical approach as CED2 and its modification with 3 diffusion tensor convolutions as CED3. If both procedures satisfy the same properties or statements, we will denote them simply CED.

3. Numerical scheme

We developed the nine-point finite volume diamond-cell scheme, see [2], [3], for the CED. The finite volume method, see [5], was chosen since a piecewise constant representation of approximate solutions in this technique is similar to the digital image structure. We were forced to switch to the nine-point method due to restrictions of the classical five-point approach, see [7], for tensor models.

Let the image be given by $n_1 \times n_2$ pixels (finite volumes) such that it seems like a square mesh with n_1 rows and n_2 columns. Let $\Omega = (0, n_1 h) \times (0, n_2 h)$ with a pixel size h. The diffusion process is considered in a time interval $I = [0, T]$. Let the time discretization be represented as $0 = t_0 \leq t_1 \leq \cdots \leq t_{N_{max}} = T$, where $t_n = t_{n-1} + k$ and k is the length of the discrete time step. We look for u^n, i.e., an approximation of solution at time t_n for every $n = 1, \ldots, N_{max}$. We start the scheme construction integrating the equation (1) over the finite volume W, then provide a semi-implicit time discretization and use the divergence theorem to acquire

$$\frac{u_W^n - u_W^{n-1}}{k} m(W) \; - \sum_{\sigma \in \mathcal{E}_W \cap \mathcal{E}_{int}} \int_\sigma \left(D^{n-1} \nabla u^n \right) \cdot \mathbf{n}_{W,\sigma} \, ds \; = \; 0, \tag{10}$$

where u_W^n represents the numerical solution at time t_n, $n = 1, \ldots, N_{max}$ on finite volume W, $W \in \mathcal{T}_h$ and $\mathcal{T}_h$ is an admissible finite volume mesh, see [5]. Further quantities and notations are given as follows: $m(W)$ is the measure of finite volume W with the boundary ∂W, $\sigma_{WE} = W \cap E$ is an edge of the

finite volume W, where $E \in \mathcal{T}_h$ is a neighbouring finite volume to W such that the measure $m(W \cap E) \neq 0$. We will use σ instead of σ_{WE} to simplify notation in places, where no confusion can appear. $\mathcal{E}_W$ is the set of edges such that $\partial W = \bigcup_{\sigma \in \mathcal{E}_W} \sigma$ and $\mathcal{E} = \bigcup_{W \in \mathcal{T}_h} \mathcal{E}_W$. $\mathcal{E}_{ext}$ represents the set of boundary edges, that is $\mathcal{E}_{ext} = \{\sigma \in \mathcal{E}, \sigma \subset \partial\Omega\}$ and $\mathcal{E}_{int} = \mathcal{E} \setminus \mathcal{E}_{ext}$. Υ denotes the set of pairs of adjacent finite volumes and is defined as

$$\Upsilon = \left\{ (W, E) \in \mathcal{T}_h^2, \ W \neq E, \ m(\sigma_{WE}) \neq 0 \right\}$$

and $\mathbf{n}_{W,\sigma}$ is the normal unit vector to σ outward to W.

Our discrete numerical solution is given as

$$u_{h,k}(x,t) = \sum_{n=0}^{N_{max}} \sum_{W \in \mathcal{T}_h} u_W^n \chi\{x \in W\}\chi\{t_{n-1} < t \leq t_n\}, \quad \chi_{\{A\}} = \begin{cases} 1, & \text{if } A \text{ is true,} \\ 0, & \text{elsewhere.} \end{cases}$$

The extension of the function $u_{h,k}(x,t)$ outside Ω is given by its periodic mirror reflection in $\Omega_\zeta = \Omega \cup B_\zeta(x)$, $x \in \partial\Omega$, where $\zeta = \max(\tilde{t}, \rho)$ for the CED2 (and $\zeta = \max(\tilde{t}, \rho, \theta)$ for the CED3) is the width of the smoothing kernel and $B_\zeta(x)$ is a circle with a center at x and a radius of ζ. Finally we extend this periodic mirror reflection by 0 outside Ω_ζ and denote it by $\tilde{u}_{h,k}$.

We start computations by defining initial values $u_W^0 = \frac{1}{m(W)} \int_W u_0(x)\, dx$, $W \in \mathcal{T}_h$. Let the finite volume approximation at the nth time step be given by

$$u_{h,k}^n(x) = \sum_{W \in \mathcal{T}_h} u_W^n \chi_{\{x \in W\}}.$$

We define an auxiliary variable $\phi_\sigma^n(u_{h,k}^n)$ which represents an approximation of the exact averaged flux $\frac{1}{m(\sigma)} \int_\sigma (D^{n-1}\nabla u^n) \cdot \mathbf{n}_{W,\sigma} ds$ for any W and $\sigma \in \mathcal{E}_W$ in order to rewrite (10) in the form

$$\frac{u_W^n - u_W^{n-1}}{k} - \frac{1}{m(W)} \sum_{\sigma \in \mathcal{E}_W \cap \mathcal{E}_{int}} \phi_\sigma^n(u_{h,k}^n)m(\sigma) = 0,$$

where $m(\sigma)$ denotes the measure of edge σ.

We propose an approximation of the flux $\phi_\sigma^n(u_{h,k}^n)$ using a co-volume mesh, see, e.g., [2], [3]. The co-volume χ_σ associated to σ is created around each edge by joining endpoints of this edge and midpoints of finite volumes which are attributed to this edge, see Fig. 2. We denote its edges as $\bar{\sigma}$. First, we build an approximation of the averaged gradient on χ_σ

$$\frac{1}{m(\chi_\sigma)} \int_{\chi_\sigma} \nabla u^n\, dx = \frac{1}{m(\chi_\sigma)} \int_{\partial\chi_\sigma} u^n \mathbf{n}_{\chi_\sigma, \bar{\sigma}}\, ds$$

$$\approx \frac{1}{m(\chi_\sigma)} \sum_{\bar{\sigma} \in \partial\chi_\sigma} \frac{u_{N_1(\bar{\sigma})}^n + u_{N_2(\bar{\sigma})}^n}{2} m(\bar{\sigma})\mathbf{n}_{\chi_\sigma, \bar{\sigma}} = p_\sigma^n(u),$$
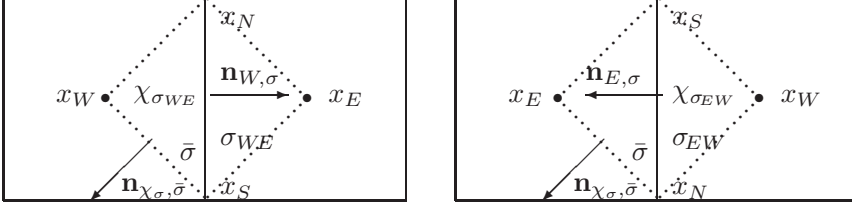
FIGURE 2. The co-volumes χ_σ associated to edges $\sigma = \sigma_{WE}$ (left) and $\sigma = \sigma_{EW}$ (right).

where $\mathbf{n}_{\chi_\sigma,\bar\sigma}$ is the normal unit vector to $\bar\sigma$ outward to χ_σ and $N_1(\bar\sigma)$ and $N_2(\bar\sigma)$ denote the endpoints of an edge $\bar\sigma \subset \partial\chi_\sigma$. u_E and u_W denote the values at x_E and x_W and the values u_N and u_S at the vertices x_N and x_S are evaluated as the arithmetic mean of neighbouring volume values (for general nonuniform meshes see [2]).

Since our mesh is uniform and squared, we can rearrange $p_\sigma^n(u)$ using the following relations: $m(\chi_\sigma) = \frac{h^2}{2}$, $m(\bar\sigma) = \frac{\sqrt{2}}{2}h$ into the form

$$p_\sigma^n(u) = \frac{u_E^n - u_W^n}{h}\mathbf{n}_{W,\sigma} + \frac{u_N^n - u_S^n}{h}\mathbf{t}_{W,\sigma}, \tag{11}$$

where $\mathbf{t}_{W,\sigma}$ is a unit vector parallel to σ such that $(x_N - x_S)\cdot\mathbf{t}_{W,\sigma} > 0$. Although u_N^n, u_W^n, u_E^n and u_S^n correspond to particular edge σ and we should denote them by $u_{N_\sigma}^n$, $u_{W_\sigma}^n$, $u_{E_\sigma}^n$ and $u_{S_\sigma}^n$ in (11) due to a simplification we omit inferior indexes σ. Replacing the exact gradient ∇u^n by the numerical gradient $p_\sigma^n(u)$ in the approximation of $\phi_\sigma^n(u_{h,k}^n)$ we have the numerical flux in the form

$$\phi_\sigma^n(u_{h,k}^n) = D_\sigma p_\sigma^n(u) \cdot \mathbf{n}_{W,\sigma}, \tag{12}$$

where

$$D_\sigma = D_\sigma^{n-1} = \begin{pmatrix} \bar{D}_{11}^\sigma & \bar{D}_{12}^\sigma \\ \bar{D}_{12}^\sigma & \bar{D}_{22}^\sigma \end{pmatrix}$$

is an approximation of the mean value of matrix D along σ evaluated at the previous time step. We evaluate the structure and diffusion tensor on σ at the point $x_{WE} = \sigma_{WE} \cap x_W x_E$.

Let us emphasise that the matrix D_σ in (12) is always considered in the basis $(\mathbf{n}_{W,\sigma}, \mathbf{t}_{W,\sigma})$, cf. [2], in order to simplify further considerations. In practice, it means that if the matrix D is given in standard basis on edge σ by

$$\begin{pmatrix} D_{11}^\sigma & D_{12}^\sigma \\ D_{12}^\sigma & D_{22}^\sigma \end{pmatrix}, \quad \text{then} \quad D_\sigma = \begin{pmatrix} D_{11}^\sigma & D_{12}^\sigma \\ D_{12}^\sigma & D_{22}^\sigma \end{pmatrix},$$

i.e., $\bar{D}_{11}^\sigma = D_{11}^\sigma$, $\bar{D}_{12}^\sigma = D_{12}^\sigma$ and $\bar{D}_{22}^\sigma = D_{22}^\sigma$ for edges parallel to the axis y.

On the other hand,

$$D_\sigma = \begin{pmatrix} D_{22}^\sigma & -D_{12}^\sigma \\ -D_{12}^\sigma & D_{11}^\sigma \end{pmatrix},$$

i.e., $\bar{D}_{11}^\sigma = D_{22}^\sigma$, $\bar{D}_{12}^\sigma = -D_{12}^\sigma$ and $\bar{D}_{22}^\sigma = D_{11}^\sigma$ for edges parallel to the axis x. Due to such a matrix representation, (12) can be rewritten in the form

$$\phi_\sigma^n(u_{h,k}^n) = \begin{pmatrix} \bar{D}_{11}^\sigma \bar{D}_{12}^\sigma \\ \bar{D}_{12}^\sigma \bar{D}_{22}^\sigma \end{pmatrix} \begin{pmatrix} \frac{u_E^n - u_W^n}{h} \\ \frac{u_N^n - u_S^n}{h} \end{pmatrix} \begin{pmatrix} 1 \\ 0 \end{pmatrix} = \bar{D}_{11}^\sigma \frac{u_E^n - u_W^n}{h} + \bar{D}_{12}^\sigma \frac{u_N^n - u_S^n}{h},$$

since the formula (11) in the basis $(\mathbf{n}_{W,\sigma}, \mathbf{t}_{W,\sigma})$ can be written for each edge as

$$p_\sigma^n(u) = \begin{pmatrix} \frac{u_E^n - u_W^n}{h} \\ \frac{u_N^n - u_S^n}{h} \end{pmatrix}$$

and $\mathbf{n}_{W,\sigma}$ in the basis $(\mathbf{n}_{W,\sigma}, \mathbf{t}_{W,\sigma})$ is equal to $\begin{pmatrix} 1 \\ 0 \end{pmatrix}$ for each edge σ.

Using the above mentioned strategy, we obtain the scheme in the form, see [3],

$$\frac{u_W^n - u_W^{n-1}}{k} - \frac{1}{m(W)} \sum_{\sigma \in \mathcal{E}_W \cap \mathcal{E}_{int}} \phi_\sigma^n(u_{h,k}^n) m(\sigma) = 0 \tag{13}$$

with

$$\phi_\sigma^n(u_{h,k}^n) = \bar{D}_{11}^\sigma \frac{u_E^n - u_W^n}{h} + \bar{D}_{12}^\sigma \frac{u_N^n - u_S^n}{h}. \tag{14}$$

We proved the convergence of the discrete solution of the scheme (13)–(14) to the weak solution of the model (1)–(3) for the CED2 in [3]. We also estimated the difference between the weak solution of the problem (1)–(3) and the approximate solution fulfilling the scheme (13)–(14) for the CED2 in dependence on the spatial and temporal discretization step, see [4]. We proved that the error of the numerical solution given by our scheme in $L_\infty(I, L_2)$ is of order h. The detailed convergence and error estimate proofs for the CED2 can be found in [3] and [4], respectively. The convergence analysis for the CED3 is our present interest of research.

4. Computational experiments

In all our experiments we use the space step h (the size of finite volume edge) equal to 0.01 and the time discretization step k of the numerical scheme (10) satisfies the relation $k = h^2$. Instead of convolution with the Gaussian kernel

$$G_t(x) = \frac{1}{4\pi t} e^{-\frac{|x|^2}{4t}}, \tag{15}$$

we apply one step of an implicit scheme solving the linear heat equation, where the relationship between the radius r of the Gaussian convolution kernel and time step k of the heat equation is given by

$$r = 3\sqrt{2k}.$$

We denote the time steps of the heat equation corresponding to three convolutions with the Gaussian kernel $G_{\tilde{t}}$, $(G_\rho$ and $G_\theta)$ by $k_{\tilde{t}}$, $(k_\rho$ and $k_\theta)$.

The first experiment shows the advantage of the CED3 in comparison to the CED2. We demonstrate it in Fig. 3.
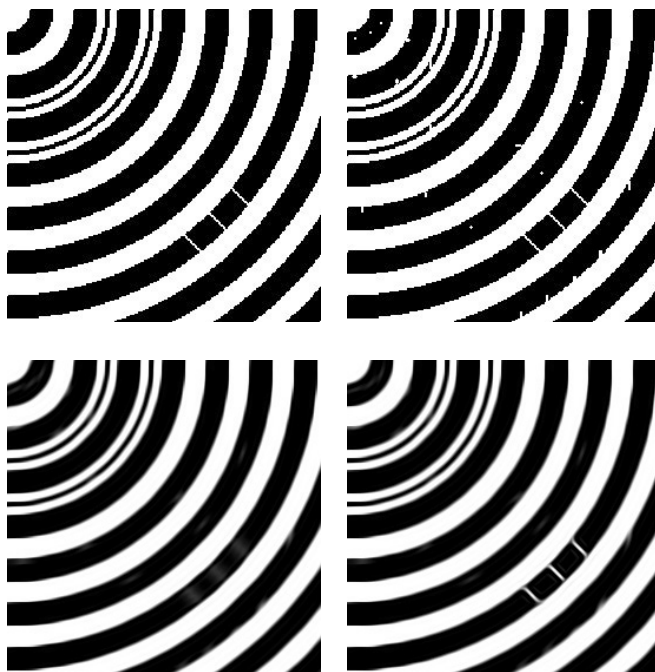

FIGURE 3. Top: the artificial image with 3 fine structures (left), the image from top, left with additional defects (right). Bottom: the image from top, right filtered by 13 steps of the CED2 (left), the image from top, right filtered by 15 steps of the CED3 (right).

We created an artificial image consisting of several wide and two narrow arcs. One of the wide arcs contains 3 fine line structures, see Fig. 3 (top, left). Then the image was damaged, see Fig. 3 (top, right), in order to compare the restoration techniques of CED2 and CED3. Our aim was to close the corrupted spots by the diffusion without the loss of 3 fine line structures. Because the fine line structures are very thin, we must choose the value of the noise scale $\tilde{t}$

very small. Otherwise, the fine structures are not recognized by the structure tensor and are consequently smoothed. The integration scale ρ must be also small to enable to preserve so tiny structures. Hence the choice of ρ is crucial for the difference between CED2 and CED3 results in this experiment. The CED2 performs in general well. Nevertheless, oscillations can appear here even if only very occasionally. To avoid them we must sufficiently enlarge the parameter ρ. Unfortunately, this enlargement often leads to loss of tiny structures. On the other hand, thanks to the third convolution, the CED3 has no problem with oscillations and hence a sufficiently small ρ can be used which enables to preserve tiny structures. The oscillations occur only if the time step k_θ of heat equation corresponds to extremely small radius of Gaussian convolution kernel G_θ, e.g., $k_\theta = 10^{-6}$ corresponds to the radius equal to 0.004. This radius is too small in comparison with the spatial step $h = 0.01$. We usually use the time step $k_\theta = 10^{-4}$ corresponding to the radius which is approximately equal to 0.042 (corresponding to 4 finite volumes). We recommend that k_θ is at least 10-times smaller than k_ρ.

We put $k_{\tilde{t}} = 2.5 \cdot 10^{-5}$ in this experiment because the use of a higher value leads to loss of fine structures. The CED3 works correctly without oscillations regardless of k_ρ selection. We chose $k_\rho = 0.002$ as the best choice satisfying the two conditions: ρ (and thus k_ρ) must be at once small so that the fine structures are recognized by the structure detector and large enough to perform sufficient diffusion. We obtained the CED3 result, see Fig. 3 (bottom, right), after 15 filtering steps using the parameter values mentioned above. CPU was 25.97 seconds. When we performed the same experiment using CED2 instead of CED3, we used the same parameter value $k_{\tilde{t}} = 2.5 \cdot 10^{-5}$ but the choice of ρ was limited by the formation of oscillations. The smallest admissible value for which the oscillations did not occur was $k_\rho = 0.0125$. Forming the oscillations is shown in Fig. 4. We used the same parameters for the CED2 and CED3: $k_{\tilde{t}} = 2.5 \cdot 10^{-5}$, $k_\rho = 0.002$ and $\alpha = 0.001$ (the parameter of diffusion tensor eigenvalues given in (7)) with the additional parameter $k_\theta = 0.0001$ for the CED3. The oscillations in the image filtered by CED2 could be observed after 15 diffusion steps, when the damaged spots were sufficiently repaired. In the next steps, they become more and more distinctive. On the other hand, in image filtered by CED3 the oscillations did not occur at all.

We used only 13 filtering steps of the CED2 to repair damaged spots in the image sufficiently because this diffusion procedure was a little faster due to larger convolution parameter k_ρ. However, the fine structures were smoothed before defect removal because this value of k_ρ is too high for so tiny structures, see Fig. 3 (bottom, left). CPU of the CED2 was 78.3 seconds which is about 3 times more than the running time of the CED3.
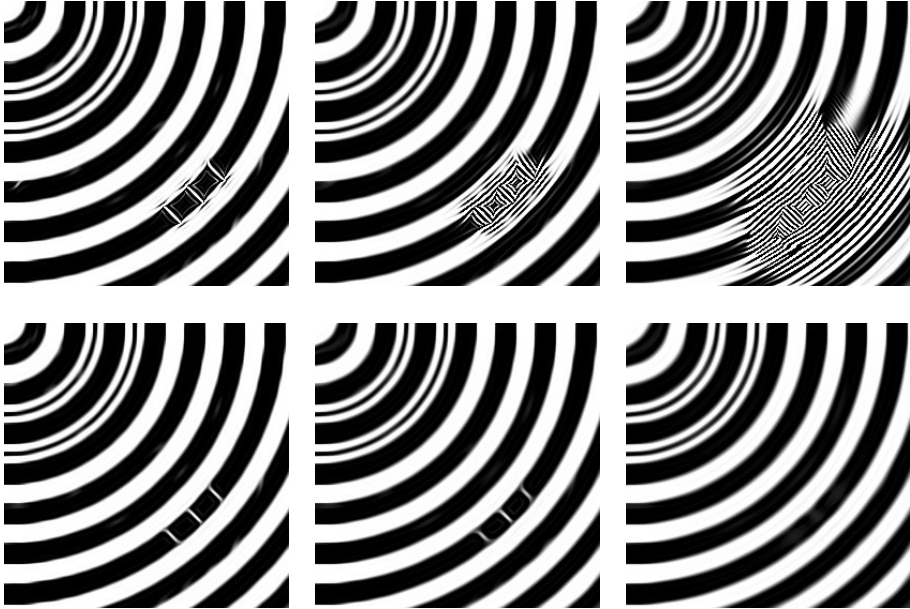
FIGURE 4. The results of CED2 (top) and CED3 (bottom) using small parameter $k_\rho = 0.002$ after 15 diffusion steps (left), after 30 steps (middle) and after 70 steps (right).
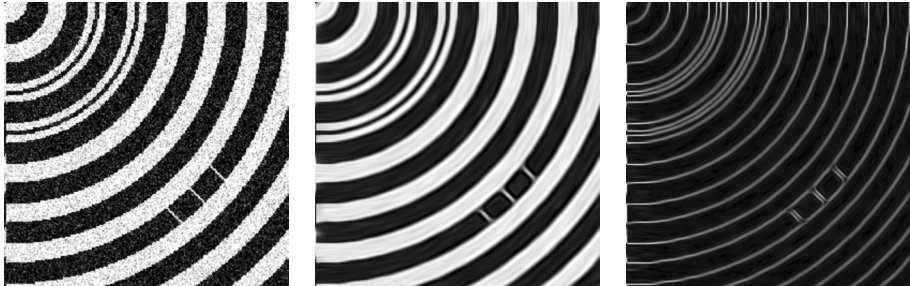
FIGURE 5. Results of the additive noise elimination. The original image (left), result after 20 time steps of the CED3 (middle), edge detection performed after 20 time steps (right).

Using the same testing image we performed experiments exploring the ability to remove additive and salt & pepper noise. The Fig. 5 and Fig. 6 show the results of applying CED3 after 20 time steps with the following set of parameters:

$$\alpha = 0.02, \quad \tilde{t} = 0.001, \quad \rho = 0.05 \quad \text{and} \quad \theta = 0.005.$$
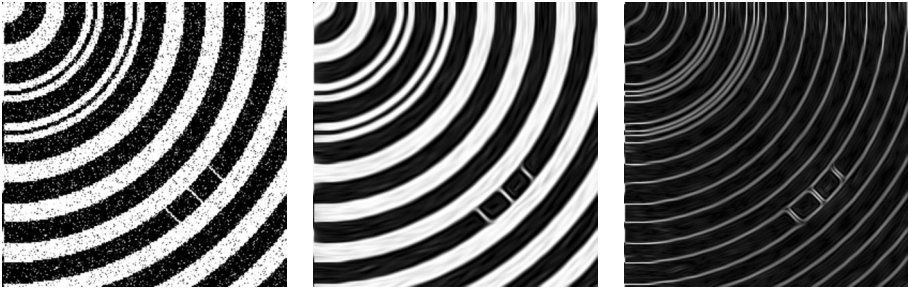
FIGURE 6. Results of the salt & pepper noise elimination. The original image (left), result after 20 time steps of the CED3 (middle), edge detection performed after 20 time steps (right).
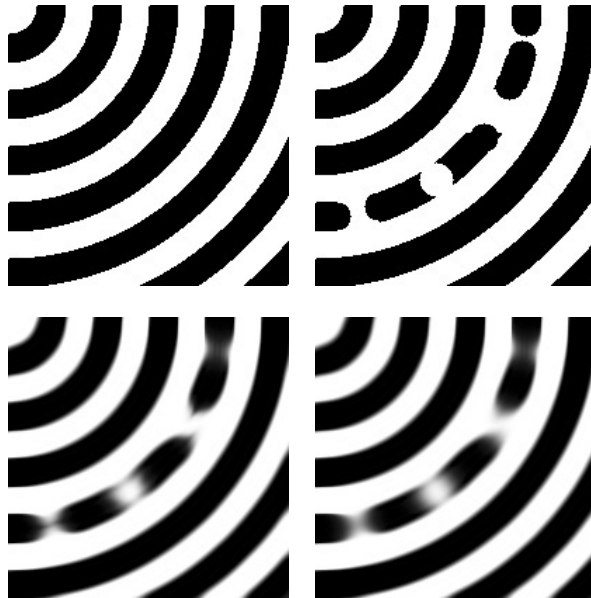

FIGURE 7. Top: the artificial image (left), the image from top, left with additional defects (right). Bottom: the image from top, right after 20 diffusion steps of the CED2 (left) and the CED3 (right).

Afterwards edge detection has been applied. Even after running more than necessary, the oscillations did not appear (however, this could happen if the parameter α to control the diffusion across edges is too small).

Several others realized experiments compared the efficiency of the CED2 and CED3. In the following text we summarize their results. If we use the same parameter values of $k_{\tilde{t}}$ and k_ρ and the same number of steps for the CED2 and CED3, the running time of CED2 is a little shorter (about 5–7 %).

However, in general a lower number of steps is sufficient for the CED3 to acquire a desirable diffusion result and hence the running time of CED3 is in fact shorter (about 10–15 %). We demonstrate this behaviour in Fig. 7.

We constructed an artificial image with wide arcs, see Fig. 7 (top, left). Then we superimposed several large interruptions in one of these arcs, see Fig. 7 (top, right). Our goal was to compare the CED2 and CED3 approaches by using the same convolution parameter values $k_{\tilde{t}}$ and k_ρ. We applied the following values: $k_{\tilde{t}} = 0.001$, $k_\rho = 0.01$ and k_θ of the CED3 equal to 0.001. We compared the results of CED2 and CED3 obtained by the same number of diffusion steps. As an example, we show the results after 20 steps, see Fig. 7 (bottom). One can see that the CED3 saturates disrupted places in the arc faster. The full arc restoration was acquired after 300 steps while the CED2 needed up to 350 steps and hence also took a longer time (about 14 %).

Next experiments show applications of the CED3. Fig. 8 shows the detail of the radar data (non-homogeneous region with tiny structures). The data was processed by the CED2 as well as CED3. Both schemes used the parameters: $k_{\tilde{t}} = 1.5 \cdot 10^{-5}$ and $\alpha = 0.005$. They differ in a choice of ρ. In the CED2 we had to apply larger k_ρ equal to 0.008 to avoid a formation of oscillations, while smaller $k_\rho = 0.001$ was sufficient for the algorithm of CED3. The parameter k_θ of the CED3 was 10-times smaller than k_ρ. We performed 8 time steps.

The coherence of the CED3 image seems to be better, moreover, while CED2 linear system needed 280 iterations, the CED3 only 45.
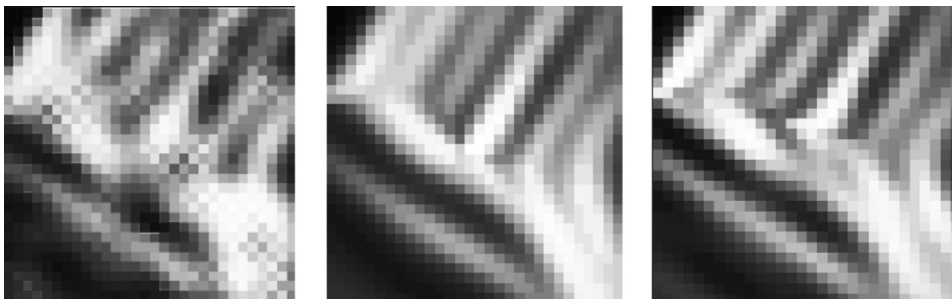
FIGURE 8. Details of the radar data (non-homogeneous region with tiny structures) processed by the CED2 and CED3. The original data is on the left, the data processed by the CED3 in the middle. To compare with the CED2 by visual inspection, its result is shown on the right.

The last experiment represents the CED as a post-processing procedure. Fig. 9 (top) shows an original (noisy) membrane image and Fig. 9 (bottom, left) the result of processing of this image by 15 time steps of the regularized (in the sense of C a t t é, L i o n s, M o r e l and C o l l) Perona-Malik equation, see [1], [8]. This diffusion model has the following form
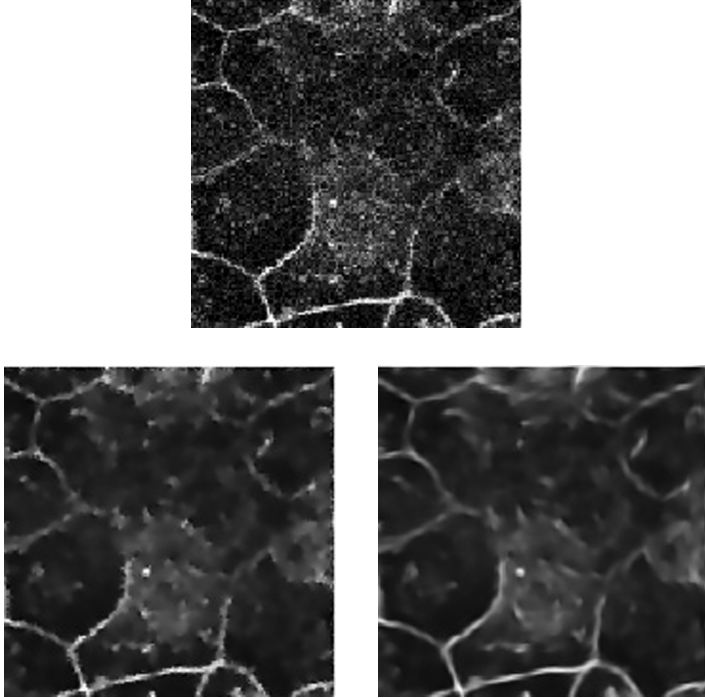

FIGURE 9. Top: the membrane original (noisy) image. Bottom: the image filtered by 15 steps of the Perona-Malik diffusion (left), the image filtered by 15 steps of the Perona-Malik diffusion and subsequently by 2 steps of the CED3 (right).

$$u_t - \nabla \cdot (g(|\nabla G_{\tilde{t}} * u|)\nabla u) \quad = \quad 0 \quad \text{in } Q_T \equiv \Omega \times I, \qquad (16)$$

$$u(x,0) \quad = \quad u_0 \ \text{in } \Omega. \qquad (17)$$

$$\nabla u \cdot \mathbf{n} \quad = \quad 0 \quad \text{on } \partial\Omega \times I. \qquad (18)$$

In our experiments we used g in the form $g(s) = \frac{1}{1+Ks^2}$. To preserve important edges, choice of large K ($K = 10$) was required to slow-down the diffusion near edges sufficiently. We obtained the image result in which the noise is blurred and image structures representing membranes are still kept, see Fig. 9 (bottom, left). However, their boundaries are rather jaggy. To improve their quality, we applied the CED3 improving the boundary coherence, see Fig. 9 (bottom, right).

5. Conclusions

The paper is devoted to the coherence enhancing diffusion. First, we briefly describe the model and show a construction of the diffusion tensor which steers the filtering process. Then we propose our regularization. The additional convolution is integrated in the model and applied to the diffusion tensor. Then we give a hint how to create the numerical scheme. The semi-implicit diamond-cell finite volume approach was used for the computational implementation. The end of section devoted to the discrete scheme contains references to fundamental theorem of the convergence and error estimate analysis for the CED2. The contribution is demonstrated in experiments showing benefits of the CED3 in comparison to the CED2.

The CED2 operates very well in practice. However, it can rarely produce oscillations due to the fact that the "out-of-diagonal" coefficients of linear system for the scheme (13)–(14) can be positive. These coefficients consist of sums and differences of the diffusion tensor elements. The oscillations appear in such diffusion processes in which both convolution kernels are very small. We can avoid a creation of oscillations in the CED2 by enlarging the convolution parameters $\tilde{t}$ and ρ (which follows from the enlargement of $k_{\tilde{t}}$ and k_ρ). However, this enlargement causes a loss of tiny structures in the image. We introduced the additional convolution in CED3 to prevent oscillations. It also enables to decrease sufficiently the parameters $\tilde{t}$ and ρ which leads to a more precise reconstruction of image edges. Thus, the diffusion procedure has no oscillation problem, additionally the third convolution leads to the filtering acceleration.

REFERENCES

[1] CATTÉ, F.—LIONS, P. L.—MOREL, J. M.—COLL, T.: *Image selective smoothing and edge detection by nonlinear diffusion,* SIAM J. Numer. Anal. **29** (1992), 182–193.

[2] COUDIERE, Y.—VILA, J. P.—VILLEDIEU, P.: *Convergence rate of a finite volume scheme for a two-dimensional convection-diffusion problem,* M2AN Math. Model. Numer. Anal. **33** (1999), 493–516.

[3] DRBLÍKOVÁ, O.—MIKULA, K.: *Convergence analysis of finite volume scheme for nonlinear tensor anisotropic diffusion in image processing,* SIAM J. Numer. Anal. **46** (2007), 37–60.

[4] DRBLÍKOVÁ, O.—HANDLOVIČOVÁ, A.—MIKULA, K.: *Error estimates of the finite volume scheme for the nonlinear tensor anisotropic diffusion,* Appl. Numer. Math. **59** (2009), 2548–2570.

[5] EYMARD, R.—GALLOUËT, T.—HERBIN, R.: *Finite volume methods.* In: *Handb. Numer. Anal.* Vol. 7 (P. G. Ciarlet et al., eds.), Elsevier, Amsterdam, 2000, pp. 713–1020.

[6] FÖRSTNER, M. A.—GÜLCH, E.: *A fast operator for detection and precise location of distinct points, corners and centres of circular features.* In: Proceedings ISPRS, Intercommission Conference on Fast Processing of Photogrammetric Data Interlakin, Switzerland, 1987, pp. 281–305.

[7] MIKULA, K.—RAMAROSY, N.: *Semi-implicit finite volume scheme for solving nonlinear diffusion equations in image processing,* Numer. Math. **89** (2001), 561–590.

[8] PERONA, P.—MALIK, J.: *Scale space and edge detection using anisotropic diffusion.* In: IEEE Transactions on Pattern Analysis and Machine Intelligence archive Vol. 12, 1990, pp. 629–639.

[9] WEICKERT, J.: *Anisotropic Diffusion in Image Processing.* Teubner, Stuttgart, Germany, 1998.

[10] ———— *Coherence-enhancing diffusion filtering,* Int. J. Comput. Vis. **31** (1999), 111–127.

[11] ———— *Coherence-enhancing diffusion of colour images,* Image Vision Comput. **17** (1999), 201–212.

Department of Mathematics and
Descriptive Geometry
Faculty of Civil Engineering
Slovak University of Technology
Radlinského 11
SK–810-05 Bratislava
SLOVAKIA
E-mail: olga.stasova@stuba.sk
zuzana.kriva@stuba.sk